Rotational intersite displacement of disordered lead atoms in a relaxor ferroelectric during piezoelectric lattice straining and ferroelectric domain switching

Shinobu Aoyagi,[1,*] Ayumi Aoyagi,[1] Hitoshi Osawa,[2] Kunihisa Sugimoto,[2,3] Yuki Nakahira,[4] Chikako Moriyoshi,[4] Yoshihiro Kuroiwa,[4] and Makoto Iwata[5]

[1]*Department of Information and Basic Science, Nagoya City University, Nagoya 467-8501, Japan*
[2]*Research and Utilization Division, Japan Synchrotron Radiation Research Institute, Sayo, Hyogo 679-5198, Japan*
[3]*Institute for Integrated Cell-Material Sciences (iCeMS), Kyoto University, Yoshida-Ushinomiya-cho, Sakyo-ku, Kyoto 606-8501, Japan*
[4]*Graduate School of Science, Hiroshima University, Higashihiroshima, Hiroshima 739-8526, Japan*
[5]*Graduate School of Engineering, Nagoya Institute of Technology, Nagoya 466-8555, Japan*

(Received 22 November 2019; revised manuscript received 24 January 2020; accepted 24 January 2020; published 18 February 2020)

We report results of the time-resolved x-ray structure analysis of a relaxor ferroelectric single crystal under an alternating electric field. The time dependence of the lattice strain, atomic displacements, and ferroelectric domain volumes in a $0.955Pb(Zn_{1/3}Nb_{2/3})O_3 - 0.045PbTiO_3$ (PZN-4.5PT) single crystal during piezoelectric lattice straining and ferroelectric domain switching is revealed. The lattice strain induced by an electric field is consistent with that expected from the piezoelectric constants. The crystal mosaicity is momentarily increased by a nucleation of nanosized ferroelectric domains when the polarization switching starts. The nucleated ferroelectric domains grow with the time constant of $\tau = 14\,\mu s$. An intersite displacement of the disordered Pb atoms observed in those site occupancies suggests that a rotational intersite displacement of Pb atoms is easily induced by an electric field and causes continuous rotation of the spontaneous polarization. The rotational intersite displacement of Pb atoms is essential for the large piezoelectric lattice strain and fatigue-free ferroelectric domain switching.

DOI: 10.1103/PhysRevB.101.064104

I. INTRODUCTION

Lead-based relaxor ferroelectrics with a composite perovskite structure, such as $(1-x)Pb(Zn_{1/3}Nb_{2/3})O_3 - xPbTiO_3$ (PZN-PT) and $(1-x)Pb(Mg_{1/3}Nb_{2/3})O_3 - xPbTiO_3$ (PMN-PT), are widely used in sensors, actuators, and transducers because of their excellent piezoelectric properties [1–3]. Their piezoelectric constants and electromechanical coupling factors are enhanced by solid solution with tetragonal $PbTiO_3$ (PT), and have the maximum value near the morphotropic phase boundary (MPB) that separates low-PT rhombohedral and high-PT tetragonal phases [4–7]. For instance, PZN-PT with $x = 0.08$ (PZN-8PT) near the MPB has the piezoelectric constant of $d_{33} = 2890\,pC/N$ and the electromechanical coupling factor of $k_{33} = 0.94$ [4–6]. The increase of the piezoelectric constants near the MPB is phenomenologically derived on the basis of a Landau-type free-energy function [8,9]. The giant electromechanical coupling of relaxor ferroelectric solid solutions has been attributed to both intrinsic and extrinsic effects [10]. The intrinsic effects are related to atomic displacements and lattice distortion of bulk crystal structure under an electric field. The extrinsic effects are related to wall motion and reorientation of nano- and mesoscale polar domains under an electric field.

Polar nanoregions (PNRs) that appear in the high-temperature paraelectric cubic phase below the Burns temperature have been believed to be responsible for the high dielectric and piezoelectric properties of relaxor ferroelectrics [11–16]. The PNRs grow on cooling and coexist with normal ferroelectric domains in the low-temperature ferroelectric rhombohedral/tetragonal phase [13]. Consequently, relaxor ferroelectrics have inhomogeneous nanoscale multidomain structures formed by PNRs, which must contribute to the extrinsic effects. Simultaneously, intrinsic effects are also important for the high piezoelectric properties of relaxor ferroelectrics [17–23]. A Rayleigh analysis of $Pb(In_{1/2}Nb_{1/2})O_3 - Pb(Mg_{1/3}Nb_{2/3})O_3 - PbTiO_3$ (PIN-PMN-PT) rhombohedral crystals revealed that 95% of the observed piezoelectric activity is intrinsic [22]. Also, recent powder x-ray diffraction (XRD) and pair-distribution function (PDF) measurements of PMN-PT ceramics under static electric field suggested that the intrinsic field-induced phase transition and polarization rotation are responsible for the high piezoelectric properties at the MPB [23]. However, the crystal structure under electric fields was not reported in that study because usual Rietveld refinement assuming a single-crystalline phase becomes invalid in the XRD measurement for a piezoelectric ceramic sample under electric fields. Crystallites in the ceramic sample with different orientations with respect to the electric-field vector will exhibit different lattice distortions and atomic displacements. Therefore, detailed intrinsic field-induced structural changes, such as atomic coordinates and atomic site occupancies under electric fields, in relaxor ferroelectrics are still unclear.

In order to reveal intrinsic field-induced structural changes of relaxor ferroelectrics, we performed the time-

*aoyagi@nsc.nagoya-cu.ac.jp

resolved x-ray structure analysis of a PZN-PT single crystal under an alternating electric field in this study. Our previous time-resolved XRD measurements under an alternating electric field have successfully revealed lattice vibrations and atomic motions in resonantly vibrating quartz and langasite-type piezoelectric single crystals [24–26]. The time-resolved single-crystal structure analyses based on a number of Bragg intensities enable simultaneous measurements of field-induced temporal changes in the lattice constants and atomic coordinates as well as volume ratios of ferroelectric domains. Observation of field-induced 180° switching of ferroelectric domains by XRD is usually difficult because Bragg intensities before and after inversion by polarization switching are almost identical according to Friedel's law. However, we have achieved simultaneous measurements of field-strength dependence of the lattice constants, atomic coordinates, and volume ratios of the ferroelectric domains in a $LiTaO_3$ single crystal by high-energy XRD under static electric fields [27]. The techniques are applied in time-resolved XRD under an alternating electric field in this study to investigate intrinsic and extrinsic structural dynamics of a relaxor ferroelectric during its piezoelectric lattice straining and ferroelectric domain switching.

II. EXPERIMENT

The time-resolved XRD for a single crystal of PZN-PT with $x = 0.045$ (PZN-4.5PT) was performed at beamline BL02B1 of the SPring-8 large synchrotron radiation facility [28]. The PZN-4.5PT single crystal with the size of $0.07 \times 0.06 \times 0.05\,mm^3$ obtained from a commercial crystal was embedded in an epoxy thin plate. Two crystal surfaces perpendicular to [001] and parallel to the epoxy thin plate were bared by polishing, and coated by an evaporated Au thin film to apply electric fields. High-energy x rays with a wavelength of $\lambda = 0.300$ Å were used to reduce absorption effects of Pb atoms. The penetration depth of x rays of 0.12 mm is larger than the crystal size. Repetitive x-ray pulses with a pulse width of 1.5 μs were extracted by a high-repetition-rate x-ray chopper [29] at a repetition rate of 4.35 kHz, and radiated on the PZN-4.5PT single crystal. The PZN-4.5PT single crystal was mechanically vibrating and alternately switching its polarization under a bipolar sine-wave electric field along [001] with an amplitude of 12 kV/cm and a frequency of 4.35 kHz, which was synchronizing with the repetitive x-ray pulses. Time-resolved XRD patterns were collected using a large cylindrical imaging plate camera by changing the delay time of the sine-wave electric field to the repetitive x-ray pulses. Time dependences of voltage and current between two electrodes on the crystal surfaces monitored by a digital oscilloscope in one period ($230\,\mu s = 1/4.35\,kHz$) are shown in Fig. 1(a). Transient positive and negative current peaks caused by polarization switching are clearly seen at times of $t = 95$ and 210 μs, respectively. The coercive field and remanent polarization along [001] obtained from the *P-E* hysteresis loop measurement at 10 Hz were 4 kV/cm and $30\,\mu C/cm^2$, respectively, which are consistent with the literature values [30]. The switching current was not decayed during the 3-day measurement. It is known that PZN-4.5PT shows no polarization fatigue below a critical field (~35 kV/cm) that induces a phase transition to a tetragonal phase [30].

III. RESULTS AND DISCUSSION

A. Field-induced lattice strain and domain switching

The rhombohedral (pseudocubic) structure of PZN-4.5PT with the space group $R3m$ is piezoelectrically deformed to a monoclinic structure with the space group m under an electric field along [001] [31,32]. There are eight kinds of ferroelectric domains i–viii with polarization along [111], $[\bar{1}11]$, $[1\bar{1}1]$, $[\bar{1}\bar{1}1]$, $[11\bar{1}]$, $[\bar{1}1\bar{1}]$, $[1\bar{1}\bar{1}]$, and $[\bar{1}\bar{1}\bar{1}]$. The lattice constant $c(a) = 4.06$ Å of the i–iv domains is increased and decreased (decreased and increased) by applying an electric field parallel to [001] and $[00\bar{1}]$, respectively [Figs. 2(a) and 2(b)]. If the absolute strength of the electric field parallel to $[00\bar{1}]$ becomes larger than the coercive field E_c, the i–iv domains are ferroelectrically switched to the v–viii domains and c (a) is increased (decreased) [Figs. 2(b) and 2(c)]. The lattice constant c (a) of the v–viii domains is increased and decreased (decreased and increased) by applying an electric field parallel to $[00\bar{1}]$ and [001], respectively [Figs. 2(c) and 2(d)]. If the absolute strength of the electric field parallel to [001] becomes larger than E_c, the v–viii domains are ferroelectrically switched to i–iv domains and c (a) is increased (decreased) [Figs. 2(d) and 2(a)].

Bragg peak positions observed in XRD patterns are shifted under an electric field by the above piezoelectric and ferroelectric effects. Figures 3(a) and 3(b) show time dependence of the 006 Bragg peak profiles parallel and perpendicular to the scattering vector $\mathbf{Q}_{006}$ [vertical and horizontal to the (001) plane], respectively. The lattice constants c were approximately estimated from the scattering vector lengths ($c = 6/Q_{006}$) and plotted with respect to time in Fig. 1(b). The time dependence of c in one period (230 μs) consists of four processes. First, c of the crystal consisting of the i–iv domains is increased and decreased by piezoelectric lattice strain according to the sine-wave electric field in the time region I from $t = -10$ to 90 μs. Second, after reaching the minimum value at $t = 90\,\mu s$, c is rapidly increased by ferroelectric domain switching from i–iv to v–viii in the time region II from $t = 90$ to 105 μs. Third, c of the crystal consisting of the v–viii domains is increased and decreased by piezoelectric lattice strain according to the sine-wave electric field in the time region III from $t = 105$ to 205 μs. Finally, after reaching the minimum value again at $t = 205\,\mu s$, c is rapidly increased by ferroelectric domain switching from v–viii to i–iv in the time region IV from $t = 205$ to 220 μs. The times when c reaches the minimum values ($t = 90$ and 205 μs) correspond to times when the current amplitude begins to increase by polarization switching in Fig. 1(a). Since the polarization p is proportional to the lattice constant c, the current density induced by polarization switching dp/dt should be proportional to dc/dt. As a result, the times when the current amplitude reaches the maximum values in Fig. 1(a) ($t = 95$ and 210 μs) correspond to times when dc/dt reaches the maximum values in Fig. 1(b). A butterfly curve is obtained by plotting the lattice constants c with respect to the electric-field strength E as shown in Fig. 1(c). The piezoelectric constant d_{33} estimated from the c butterfly curve is 2.1×10^3 pC/N, which is consistent with the literature value of $> 2 \times 10^3$ pC/N measured by the resonance method [33]. Therefore, the piezoelectricity of PZN-4.5PT is basically explained in terms of intrinsic effects.

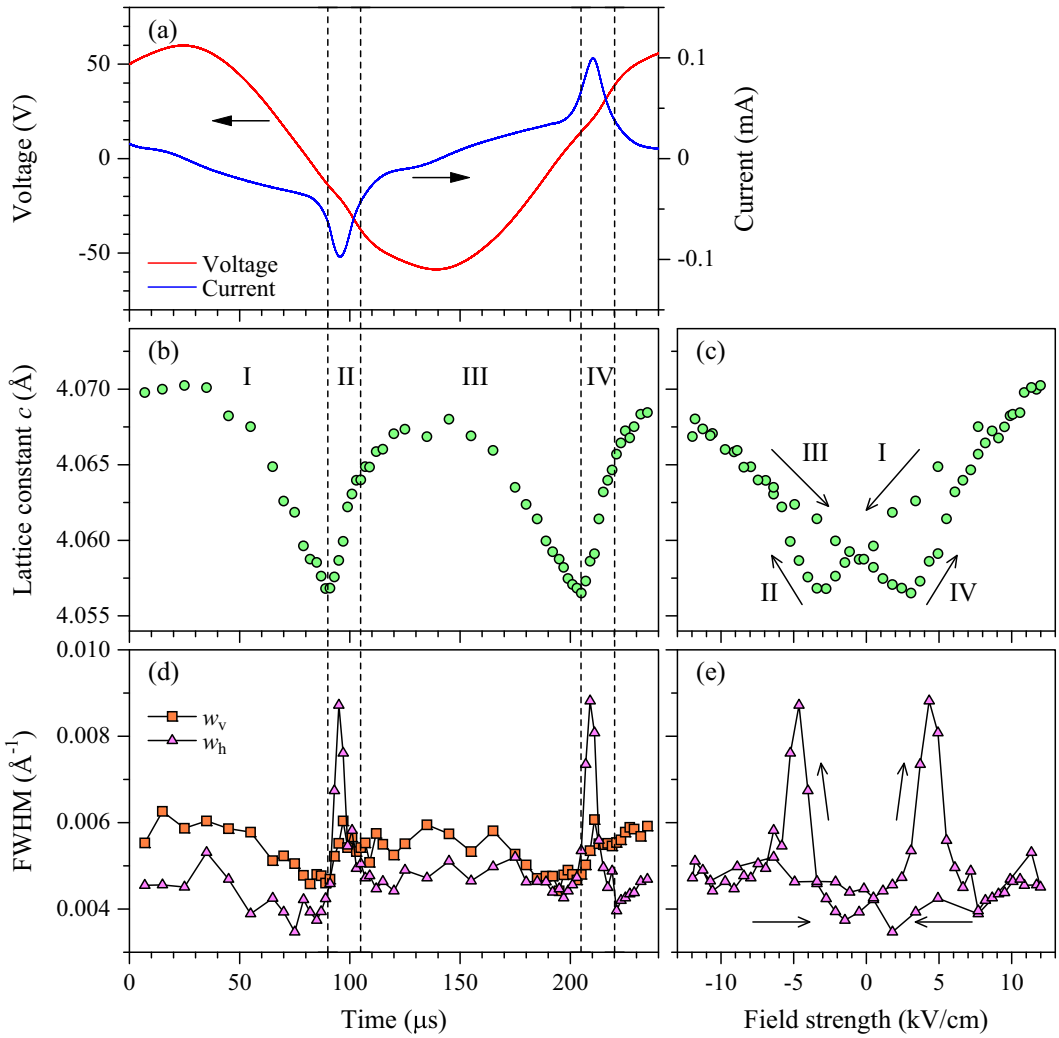

FIG. 1. Time dependences of (a) the voltage (red) and the current (blue) between two electrodes on the crystal surfaces, (b) the lattice constant c, and (d) the FWHM of the 006 Bragg peak parallel (square) and perpendicular (triangle) to the scattering vector. (c) Field-strength dependence of the lattice constant c obtained from (a), (b). (e) Field-strength dependence of the FWHM of the 006 Bragg peak perpendicular to the scattering vector obtained from (a), (d).

The 006 Bragg peak profile perpendicular to $\mathbf{Q}_{006}$ at $t = 95$ μs is exceptionally broader as shown in Figs. 3(a) and 3(b). The full widths at half maximum (FWHM) of the profiles parallel (w_v) and perpendicular (w_h) to $\mathbf{Q}_{006}$ were obtained by least-squares fitting using a pseudo-Voigt function, and plotted with respect to time in Fig. 1(d). Both w_v and w_h slightly decrease with decrease of c and p in the time regions I and III. The peak sharpening would be caused by ease of lattice strain and mismatch on boundaries between ferroelectric i–iv (or v–viii) domains accompanied with decreases of polarization p. After w_v, w_h, and c reach the minimum values at $t = 90$ and 205 μs, w_h rapidly increases and decreases within 10 μs. The times when w_h reaches the maximum at $t = 95$ and 210 μs agree with the times when the current amplitude reaches the maximum [Fig. 1(a)]. Similar transient increase of a Bragg peak width during polarization switching has been observed in a $Pb(Zr_{0.2}Ti_{0.8})O_3$ thin film and a $Sr_{0.5}Ba_{0.5}Nb_2O_6$ single crystal by time-resolved XRD measurements [34,35]. Figure 1(e) shows field-strength dependence of w_h. The increase of w_h observed in Figs. 1(d) and 1(e) indicates increase of mosaicity of the crystal during polarization switching. This behavior is explained by a nanoscale multidomain structure formed by random nucleation of polarization-reversed and misoriented v–viii (or i–vi) domains in parent i–iv (or v–viii) domains. In contrast, w_v shows almost no peak broadening. This means that the nucleated and parent domains have nearly identical lattice constants during polarization switching. Therefore, the polarization-reversed domains with the inverted crystal structure are nucleated without lattice mismatch, but with lattice misorientation. Nucleated v, vi, vii, and viii domains have lattices matched with lattices of their 180° domains that are parent iv, iii, ii, and i domains, respectively (Fig. 2). There are six kinds of domain boundaries in the time region I: i/ii, i/iii, i/iv, ii/iii, ii/iv, and iii/iv. Domains v, vi, vii, and viii would be nucleated in domains i, ii, iii, and iv, respectively, during polarization switching in time region II. The nuclei of v, vi, vii, and viii are easily formed without lattice mismatch on domain boundaries between iv, iii, ii, and i, respectively. This transient domain structure would contribute to fatigue-free polarization switching.

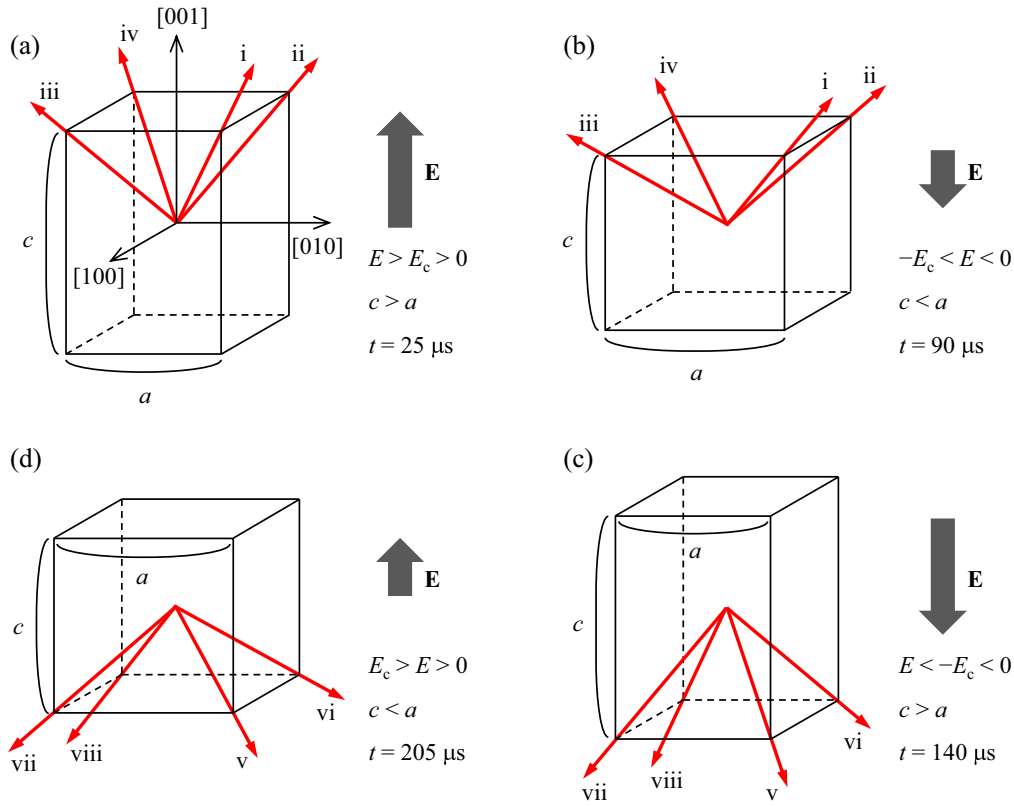

FIG. 2. Schematic time dependence of polarization orientations of the eight domains i–viii (red arrows) and lattice strain of the pseudocubic unit cell under the alternating electric field at t = (a) 25, (b) 90, (c) 140, and (d) 205 μs.

Polarization-reversed domains grow after the nucleation to govern the whole crystal. Figure 3(c) shows time dependence of the 544 Bragg peak profile parallel to the scattering vector $\mathbf{Q}_{544}$. The 544 Bragg peak is split into two peaks by domain twinning in the rhombohedral phase. Domain i with a lattice elongated along [111] and remaining domains ii–iv contribute to the left and right peaks, respectively, in the time region I. Domains i, ii, iii, and iv would be switched to domains v, vi, vii, and viii, respectively, by applying an electric field parallel to [00$\bar{1}$] above the coercive field in time region II [Figs. 2(b) and 2(c)]. Consequently, domain viii with a lattice elongated along [111] and remaining domains v–vii contribute to the left and right peaks, respectively, in time region III. If volume ratios of i–iv (v–viii) domains are constantly equal to 0.25 in time region I (III), the intensity ratio between the left and right peaks is almost unchanged through the piezoelectric lattice strain and polarization switching according to Friedel's law. However, the left peak that is larger than the right peak before $t = 95\,\mu$s changes to be smaller after $t = 95\,\mu$s as shown in Fig. 3(c). Changes in the peak shape and intensity ratio between the two peaks in time region I relate to domain switching accompanied with piezoelectric lattice strain, which would contribute to extrinsic effects. Changes in the peak shape and intensity ratio between the two peaks in time region II relate to domain nucleation and growth accompanied with ferroelectric polarization switching. The distance between the two peaks relating to the lattice angles is almost unchanged during the piezoelectric lattice strain and ferroelectric domain switching. The rhombohedral lattice angle calculated from the distance between the two peaks is $\alpha = 89.94(1)^\circ$.

B. Field-induced rotational intersite displacement of Pb atoms

Time dependences of the volume ratios of domains and the crystal structure were investigated by structure analyses based on integrated intensities of ~1500 independent Bragg peaks (d spacing >0.45 Å) at $t = 25$, 65, 85, 92, 95, 97, 99, 101, and 140 μs. Intensities of Bragg peaks split and overlapped by domain twinning were integrated to obtain sums of integrated intensities of multiple domains. A Pb-disordered structure model was used in the structure analysis because it gave better reliability factors than a Pb-ordered structure model. A Pb atom partially occupies four fractional positions in the unit cell with polarization along [111], Pb(1) : $(\Delta x_{Pb}, \Delta x_{Pb}, \Delta x_{Pb})$, Pb(2) : $(\Delta x_{Pb}, \Delta x_{Pb}, -\Delta x_{Pb})$, Pb(3) : $(\Delta x_{Pb}, -\Delta x_{Pb}, \Delta x_{Pb})$, and Pb(3′) : $(-\Delta x_{Pb}, \Delta x_{Pb}, \Delta x_{Pb})$. Pb(3) and Pb(3′) are equivalent in the deformed monoclinic structure. The Pb displacement from the origin (Δx_{Pb}) and the site occupancy at Pb(1) (g_{Pb1}) were determined as $\Delta x_{Pb} = 0.039$ and $g_{Pb1} = 0.264$, respectively, using the data at $t = 25\,\mu$s, and fixed to simplify the structure model for the systematic analysis. Chemically disordered Zn, Nb, and Ti atoms occupy the body centered position (0.5, 0.5, 0.5) without positional disorder. O atoms occupy near the face centered positions, O(1) : $(0.5 + \Delta x_{O1}, 0.5 + \Delta x_{O1}, \Delta z_{O1})$, O(2) : $(0.5 + \Delta x_{O2}, \Delta y_{O2}, 0.5 +$

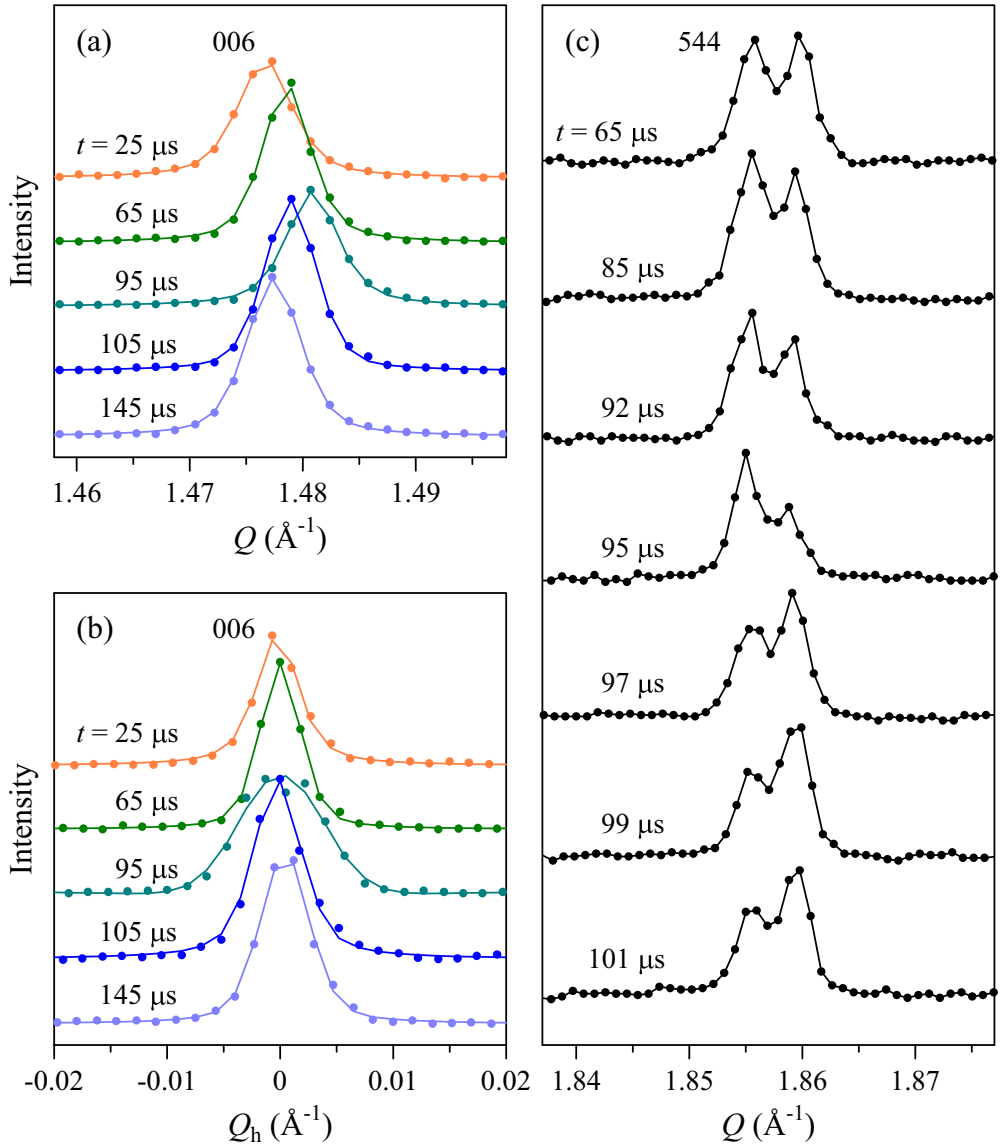

FIG. 3. Time dependences of the 006 Bragg peak profile (a) parallel and (b) perpendicular to the scattering vector $\mathbf{Q}_{006}$ and (c) the 544 Bragg peak profile parallel to the scattering vector $\mathbf{Q}_{544}$. Q is the scattering vector length in (a), (c). Q_h is the scattering vector component perpendicular to $\mathbf{Q}_{006}$ in (b). Solid lines in (a), (b) show least-square fits by a pseudo-Voigt function.

Δz_{O2}), and O(2′) : (Δy_{O2}, 0.5 + Δx_{O2}, 0.5 + Δz_{O2}) without positional disorder. O(2) and O(2′) are equivalent in the deformed monoclinic structure. Volume ratios of domains (D_{i-viii}), site occupancies of the disordered Pb atom, atomic coordinates of the O atoms, and anisotropic atomic displacement parameters (U_{ij}) of all atoms were refined by full-matrix least-squares analysis using SHELXL [36]. Results of the structure analyses are summarized in Tables I–III. Figure 4(a) shows the refined Pb-disordered monoclinic structure model at $t = 25\,\mu$s. An XRD data set obtained under zero field ($\lambda = 0.301$ Å, d spacing > 0.45 Å) was also analyzed using a similar Pb-disordered rhombohedral structure model. Pb(3) [Pb(3′)] and O(2) [O(2′)] become equivalent to Pb(2) and O(1), respectively, in the zero-field rhombohedral structure model.

As a result of investigation of time dependences of the refined parameters, significant temporal changes were found in the site occupancies of Pb(2) and Pb(3) (g_{Pb2} and g_{Pb3}) as shown in Fig. 5(a). g_{Pb2} and g_{Pb3} are decreased and increased with increase of the lattice constant c [Fig. 1(b)], respectively. Ferroelectric $LiTaO_3$ exhibits no changes in atomic structure parameters even under a static electric field of 180 kV/cm [27]. In contrast, g_{Pb2} and g_{Pb3} in PZN-4.5PT respond sensitively to the alternating electric field with amplitude of 12 kV/cm. The significant changes in g_{Pb2} and g_{Pb3} are expressed by a rotational intersite displacement of a Pb atom as shown in Figs. 4(b) and 4(c). The Pb(1)-Pb(2) and Pb(1)-Pb(3) intersite distances are both 0.32 Å and comparable to $2\sqrt{U_{eq}(Pb)} = 0.31$ Å, where U_{eq}(Pb) is the average of the equivalent isotropic atomic displacement parameters of Pb(1), Pb(2), and Pb(3). Therefore, intersite displacement of a Pb atom among the four disordered sites [Pb(1), Pb(2), Pb(3), and Pb(3′)] can be easily induced by thermal and electric excitation. The oxygen displacements along the electric field

TABLE I. Summary of the crystal structure analyses of PZN-4.5PT under the alternating electric field and zero field. N, n, R, R_w, and S are the number of independent Bragg intensities used in the analysis, the number of refined parameters, the reliability factor based on absolute structure factors, the weighted reliability factor based on squared structure factors, and the least-squares goodness-of-fit parameter, respectively. The lattice constants a and c were determined by the least-squares refinement on hundreds of Bragg peak positions recorded on one oscillation photograph. The lattice angles α, β, and γ [$\sim$89.94(1)°] were not refined due to the pseudomerohedral twinned structure.

	E (kV/cm)	a (Å)	c (Å)	N	n	R	R_w	S
$t(\mu s) = 25$	12.0	4.0576(1)	4.0714(1)	1559	41	0.0300	0.0634	1.030
65	4.9	4.0603(1)	4.0660(1)	1572	39	0.0350	0.0647	0.976
85	−1.5	4.0636(1)	4.0589(1)	1570	39	0.0344	0.0632	0.978
92	−3.7	4.0650(1)	4.0562(1)	1570	39	0.0324	0.0639	1.032
95	−4.6	4.0645(1)	4.0574(1)	1569	39	0.0337	0.0646	1.017
97	−5.2	4.0639(1)	4.0586(1)	1568	39	0.0340	0.0624	0.952
99	−5.8	4.0632(1)	4.0602(1)	1572	39	0.0325	0.0620	0.957
101	−6.4	4.0623(1)	4.0616(1)	1571	39	0.0334	0.0626	0.944
140	−12.0	4.0592(1)	4.0668(1)	1552	39	0.0325	0.0672	1.067
zero-field	0	4.0630(1)		601	19	0.0175	0.0462	1.085

TABLE II. Atomic coordinates and site occupancies of PZN-4.5PT under the alternating electric field and zero field.

	Δx_{Pb}	g_{Pb1}	g_{Pb2}	g_{Pb3}	Δx_{O1}	Δz_{O1}	Δx_{O2}	Δy_{O2}	Δz_{O2}
$t(\mu s) = 25$	0.039(1)	0.264(6)	0.216(6)	0.260(3)	−0.023(1)	−0.019(2)	−0.024(2)	−0.015(2)	−0.028(2)
65	0.039	0.264	0.232(5)	0.252(3)	−0.023(2)	−0.019(3)	−0.024(1)	−0.015(1)	−0.025(2)
85	0.039	0.264	0.254(5)	0.241(3)	−0.025(2)	−0.012(3)	−0.026(1)	−0.017(1)	−0.016(2)
92	0.039	0.264	0.255(5)	0.241(3)	−0.026(2)	−0.012(3)	−0.026(1)	−0.016(1)	−0.019(3)
95	0.039	0.264	0.253(5)	0.242(3)	−0.025(2)	−0.013(3)	−0.025(1)	−0.016(1)	−0.014(3)
97	0.039	0.264	0.245(5)	0.245(3)	−0.024(2)	−0.010(3)	−0.026(2)	−0.017(2)	−0.013(2)
99	0.039	0.264	0.247(5)	0.245(3)	−0.023(2)	−0.009(3)	−0.024(1)	−0.015(1)	−0.015(2)
101	0.039	0.264	0.246(5)	0.245(3)	−0.023(2)	−0.008(3)	−0.023(1)	−0.015(1)	−0.015(2)
140	0.039	0.264	0.213(5)	0.262(3)	−0.024(2)	−0.010(3)	−0.020(2)	−0.013(2)	−0.019(2)
zero-field	0.039	0.22(2)	0.259(6)		−0.022(1)	−0.015(1)			

TABLE III. Anisotropic atomic displacement parameters (10^{-3} Å^2) of PZN-4.5PT under the alternating electric field and zero field. U_{ij} (ij = 11, 22, 33, 23, 13, and 12) are shown for each atom site. U_{22} and U_{13} of atoms on the mirror plane [Pb(1), Pb(2), Zn/Nb/Ti, and O(1)] and U_{33} and U_{12} of atoms on the threefold axis [Pb(1) and Zn/Nb/Ti at zero field], which are equal to U_{11} and U_{23}, respectively, are omitted.

	Pb(1)	Pb(2)	Pb(3)	Zn/Nb/Ti	O(1)	O(2)
$t(\mu s) = 25$	15(1), 17(2), −3(2), 0(2)	26(2), 23(2), −3(2), −10(2)	39(2), 20(1), 36(2), 3(2), −24(2), 6(2)	11(1), 11(1), −3(1), 1(1)	26(2), 15(2), −2(2), −7(3)	26(2), 14(2), 26(2), −1(3), −6(3), 3(2)
65	20(2), 20(3), −6(2), −9(2)	24(2), 24(2), −3(2), −5(2)	34(2), 20(1), 33(2), 1(2), −20(2), 2(1)	10(1), 10(1), −3(1), 1(1)	27(2), 13(2), 2(3), −6(4)	26(2), 14(1), 26(3), −2(3), −5(3), −1(2)
85	19(2), 26(3), −8(2), −6(2)	26(2), 20(2), −1(2), −11(2)	34(2), 21(1), 29(2), 0(2), −17(2), 2(1)	10(1), 9(1), −3(1), −1(1)	27(2), 17(2), −1(4), −4(4)	27(2), 13(1), 30(3), −3(4), −8(4), 1(2)
92	20(2), 25(3), −8(2), −7(2)	26(2), 18(2), −1(1), −11(2)	32(2), 21(1), 30(2), 2(2), −15(2), 1(1)	10(1), 9(1), −3(1), −1(1)	25(2), 16(2), −1(4), −6(3)	27(2), 15(2), 27(3), −3(4), −5(4), −3(2)
95	20(2), 28(3), −10(2), −4(2)	27(2), 18(2), 1(1), −14(2)	31(2), 21(1), 28(2), −1(2), −11(2), 2(1)	10(1), 9(1), −2(1), 0(1)	25(2), 18(3), −4(4), −5(3)	26(2), 16(2), 29(3), −4(5), −8(5), −3(2)
97	21(2), 25(3), −10(2), −6(2)	25(2), 19(2), 0(1), −11(2)	31(2), 21(1), 31(2), −1(2), −11(2), 2(1)	10(1), 9(1), −3(1), −1(1)	26(2), 17(2), 1(4), −9(4)	27(2), 14(2), 33(3), −6(5), −6(5), 1(2)
99	22(2), 27(3), −11(2), −6(2)	24(2), 20(2), 1(1), −11(2)	31(2), 20(1), 29(2), 0(2), −9(2), 2(1)	10(1), 9(1), −2(1), 0(1)	27(2), 18(2), −1(4), −9(4)	28(2), 14(2), 30(3), −6(4), −8(4), −2(2)
101	23(2), 27(3), −10(2), −7(2)	25(2), 19(2), 1(2), −10(2)	31(2), 20(1), 28(2), 0(2), −9(2), 2(1)	10(1), 9(1), −2(1), 0(1)	26(2), 16(2), −3(4), −6(4)	27(2), 14(2), 33(3), −8(4), −6(5), −2(2)
140	24(2), 21(2), −4(2), −11(2)	22(2), 20(2), 10(2), −3(2)	31(2), 21(1), 36(2), −5(1), −11(2), 2(1)	10(1), 10(1), 1(1), 0(1)	26(2), 20(2), 1(4), −8(4)	29(2), 15(2), 32(3), −9(5), −9(5), −1(3)
zero-field	20(2), 1(2)	31(1), 22(1), 3(1), −19(1)		12(1), 1(1)	29(1), 16(1), −1(2), −6(2)	

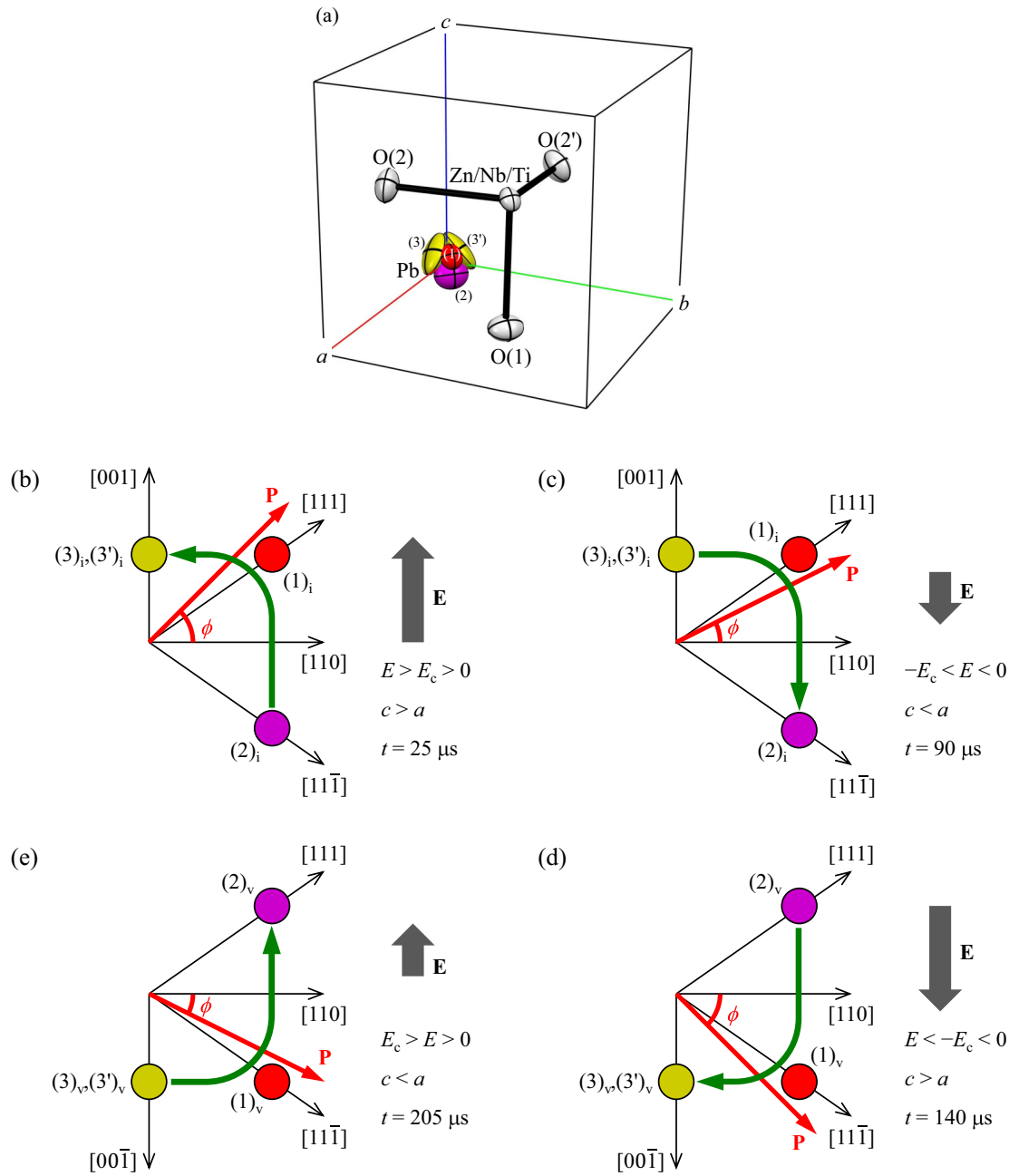

FIG. 4. (a) Pb-disordered monoclinic structure model at $t = 25\,\mu$s with atomic displacement ellipsoids at 50% probability level. The Pb(1) (red), Pb(2) (purple), Zn/Nb/Ti, and O(1) sites are on the $(1\bar{1}0)$ crystallographic mirror plane. Pb(3) (yellow) and O(2) sites are equivalent with Pb(3′) (yellow) and O(2′) sites, respectively, by the mirror symmetry. (b)–(e) Schematic drawings of the rotational intersite displacement of a Pb atom under the alternating electric field at $t =$ (a) 25, (b) 90, (c) 140, and (d) 205 μs viewed along $[1\bar{1}0]$. Red, purple, and yellow circles represent Pb(1), Pb(2), and Pb(3) [Pb(3′)], respectively. Green arrows represent directions of the rotational intersite displacement of a Pb atom. Red arrows represent the polarization orientation vectors **P** from the origin in the unit cell through the barycenter of the disordered Pb atom.

from $t = 25\,\mu$s with the maximum c value to $t = 92\,\mu$s with the minimum c value were only 0.03(2) Å for O(1) and 0.04(2) Å for O(2). The rotational intersite displacement of Pb atoms easily induced by electric fields is responsible for the high piezoelectric properties and the giant electromechanical coupling.

It is naturally expected that domains i, ii, iii, and iv in time region I are switched to domains v, vi, vii, and viii in time region II, respectively [Figs. 2(b) and 2(c)]. Certainly, sums of refined volume ratios of the mutually switchable domain pairs ($D_{\rm i} + D_{\rm v}$, $D_{\rm ii} + D_{\rm vi}$, $D_{\rm iii} + D_{\rm vii}$, and $D_{\rm iv} + D_{\rm viii}$) are almost constant within errors with respect to time. The time-averaged values are 0.30(6) for $D_{\rm i} + D_{\rm v}$, 0.21(4) for $D_{\rm ii} + D_{\rm vi}$, 0.21(4) for $D_{\rm iii} + D_{\rm vii}$, and 0.28(6) for $D_{\rm iv} + D_{\rm viii}$. In contrast, the sum of refined volume ratios of domains v–viii (i–iv), which is close to 0 and 1 (1 and 0) in the

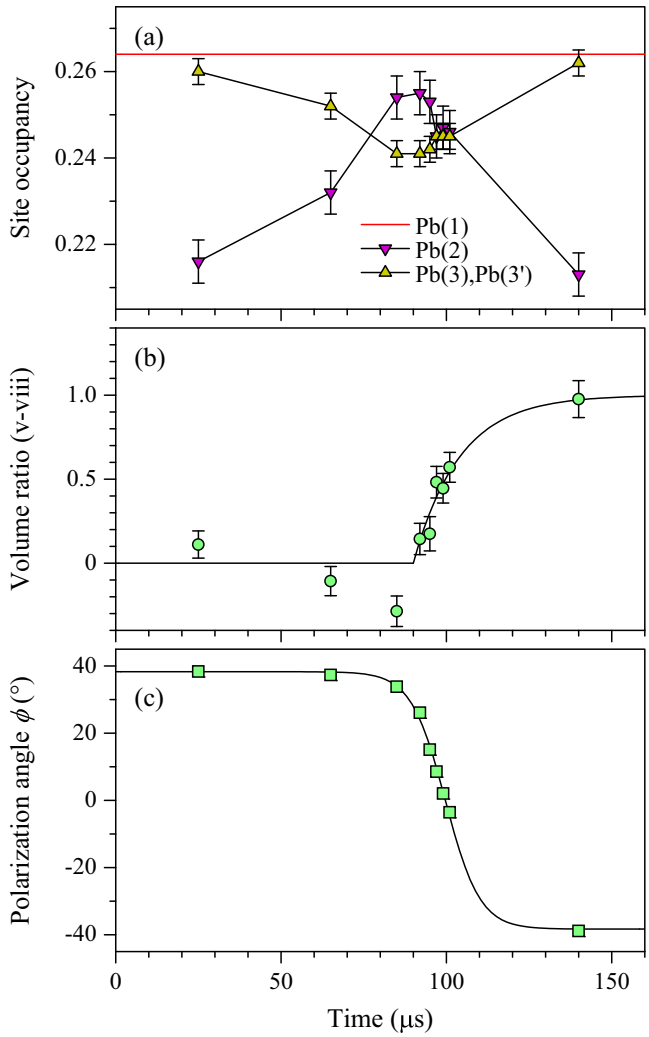

FIG. 5. Time dependences of (a) the site occupancies of Pb(2) (downward triangle) and Pb(3) (upward triangle), (b) the volume ratio of the domains v–viii, and (c) the average polarization angle ϕ in mutually switchable two domains. The red line in (a) shows the fixed site occupancy of Pb(1).

time region I and III, respectively, increases (decreases) with respect to time in time region II as shown in Fig. 5(b). The volume ratios of v−viii($D_v + D_{vi} + D_{vii} + D_{viii}$) in time region II from $t = 90\,\mu$s was fitted by the exponential growth function $1 - \exp[(90 - t)/\tau]$ with the time constant $\tau = 14\,\mu$s.

The i–v (ii–vi, iii–vii, and iv–viii) domain switching involves rotational intersite displacement of the disordered Pb atoms as shown in Figs. 4(b)–4(e). $Pb(1)_i$ and $Pb(2)_i$ sites in domain i [Figs. 4(b) and 4(c)] correspond to $Pb(2)_v$ and $Pb(1)_v$ sites in domain v [Figs. 4(d) and 4(e)], respectively. $Pb(3)_i$ and $Pb(3')_i$ sites in domain i are not occupied in domain v. $Pb(3)_v$ and $Pb(3')_v$ sites in domain v are not occupied in domain i. Fractions of Pb atoms at $Pb(1)_i$, $Pb(2)_i$, $Pb(3)_i$, $Pb(1)_v$, $Pb(2)_v$, and $Pb(3)_v$ are given by $g_{Pb1}D_i$, $g_{Pb2}D_i$, $g_{Pb3}D_i$, $g_{Pb1}D_v$, $g_{Pb2}D_v$, and $g_{Pb3}D_v$, respectively. g_{Pb1} and g_{Pb2} are 0.264 and $1 - (g_{Pb1} + 2g_{Pb3}) = 0.736 - 2g_{Pb3}$ in the structure model, respectively. D_i and D_v are fitted by $\exp[(90 - t)/\tau]$ and $1 - \exp[(90 - t)/\tau]$ in time region II, respectively. Therefore, domain switching from i to v is explained by the rotational intersite displacement of Pb atoms from $Pb(3)_i$ and $Pb(3')_i$ to $Pb(2)_v$, from $Pb(1)_i$ to $Pb(1)_v$, and from $Pb(2)_i$ to $Pb(3)_v$ and $Pb(3')_v$ [Figs. 4(c) and 4(d)]. Inversely, domain switching from v to i is explained by the rotational intersite displacement of Pb atoms from $Pb(3)_v$ and $Pb(3')_v$ to $Pb(2)_i$, from $Pb(1)_v$ to $Pb(1)_i$, and from $Pb(2)_v$ to $Pb(3)_i$ and $Pb(3')_i$ [Figs. 4(e) and 4(b)]. The oxygen displacements caused by the domain switching [0.10 Å for O(1) and 0.15 Å for O(2)] are much smaller than the Pb(1)-Pb(2) and Pb(1)-Pb(3) intersite displacements (0.32 Å). This structural feature enables easy switching and rotation of the large polarization by the rotational intersite displacement of Pb atoms with a small lattice distortion. Therefore, the rotational intersite displacement of Pb atoms is essential for the fatigue-free domain and polarization switching.

The polarization orientation in each domain changes with the field-induced lattice strain and domain switching. The polarization orientation is assumed to be parallel to a vector **P** from the origin in the pseudocubic unit cell through the barycenter of the disordered Pb atom. The angle ϕ between the vector **P** and the [110] direction is increased when the site occupancies of Pb(2) and Pb(3) are decreased and increased, respectively, in domains i and v [Figs. 4(b)–4(e)]. Domains i and v under zero field have polarizations along [111] with $\phi = 35^\circ$ and [11$\bar{1}$] with $\phi = -35^\circ$, respectively. Average polarization orientations in mutually switchable two domains (e.g., i and v) were calculated from the lattice constants [Fig. 1(b)], the site occupancies of disordered Pb [Fig. 5(a)], and the exponential growth function of domain switching [Fig. 5(b)]. Figure 5(c) shows time dependence of calculated ϕ angles of the average polarization orientations. The polarization with $\phi = 38^\circ$ at $t = 25\,\mu$s begins to decrease around $t = 80\,\mu$s and becomes zero at $t = 100\,\mu$s when the switched domain-volume ratio becomes 0.5. After that, ϕ becomes negative and reaches $\phi = -38^\circ$ at $t = 140\,\mu$s. The continuous field-induced polarization rotation during the piezoelectric lattice strain and ferroelectric domain switching is achieved by the rotational intersite displacement of Pb atoms.

IV. CONCLUSIONS

We have revealed the transient lattice strain, atomic displacements, and domain nucleation and growth in a PZN-4.5PT single crystal during its piezoelectric lattice straining and ferroelectric domain switching by time-resolved x-ray structure analysis under an alternating electric field. The large lattice strain observed under the electric field suggests that the piezoelectricity of PZN-4.5PT is basically explained in terms of intrinsic effects. Nanoscale ferroelectric domains which increase crystal mosaicity are nucleated without lattice mismatch but with lattice misorientation when the electric-field strength reaches the coercive field. The nucleated ferroelectric domains grow with the time constant of $\tau = 14\,\mu$s. The large piezoelectric lattice strain and fatigue-free ferroelectric domain switching are caused by the rotational intersite displacement of disordered Pb atoms, which is easily induced by an electric field and enables continuous rotation

of the spontaneous polarization. The local potential structure of the Pb atoms is critical for the outstanding piezoelectric and ferroelectric properties in the present scenario. It is expected that the number of the disordered Pb sites is increased and the intersite potential barrier is lowered in the low-symmetry monoclinic PZN-9.0PT at the MPB [37]. The atomic motion of the Pb atoms induced by an alternating electric field in relaxor ferroelectrics near the MPB should be investigated by the technique used in this study for deeper understanding of the mechanism of the high piezoelectric properties.

ACKNOWLEDGMENTS

This work was supported by a Grant-in-Aid for Scientific Research from the Japan Society for the Promotion of Science (JSPS) (Grants No. 26870491 and No. 16K05017), Toyoaki Scholarship Foundation, Daiko Foundation, and the Research Equipment Sharing Center at the Nagoya City University. The synchrotron radiation experiments were performed at SPring-8 with the approval of the Japan Synchrotron Radiation Research Institute (JASRI) (Proposals No. 2015A0100, No. 2015B0100, No. 2016A1328, No. 2017B1976, and No. 2019B1470).

[1] R. A. Cowley, S. N. Gvasaliya, S. G. Lushnikov, B. Roessli, and G. M. Rotaru, Adv. Phys. **60**, 229 (2011).
[2] S. Zhang and F. Li, J. Appl. Phys. **111**, 031301 (2012).
[3] E. Suna and W. Cao, Prog. Mater. Sci. **65**, 124 (2014).
[4] J. Kuwata, K. Uchino, and S. Nomura, Jpn. J. Appl. Phys. **21**, 1298 (1982).
[5] S.-E. Park and T. R. Shrout, J. Appl. Phys. **82**, 1804 (1997).
[6] R. Zhang, B. Jiang, W. Jiang, and W. Cao, IEEE Trans. Ultrason., Ferroelectr., Freq. Control **49**, 1622 (2002).
[7] Y. Guo, H. Luo, D. Ling, H. Xu, T. He, and Z. Yin, J. Phys.: Condens. Matter **15**, L77 (2003).
[8] Y. Ishibashi and M. Iwata, Jpn. J. Appl. Phys. **37**, L985 (1998).
[9] Y. Ishibashi and M. Iwata, Jpn. J. Appl. Phys. **38**, 800 (1999).
[10] L. Bellaiche and D. Vanderbilt, Phys. Rev. Lett. **83**, 1347 (1999).
[11] R. Pirc, R. Blinc, and V. S. Vikhnin, Phys. Rev. B **69**, 212105 (2004).
[12] G. Y. Xu, J. S. Wen, C. Stock, and P. M. Gehring, Nat. Mater. **7**, 562 (2008).
[13] D. Fu, H. Taniguchi, M. Itoh, S.-Y. Koshihara, N. Yamamoto, and S. Mori, Phys. Rev. Lett. **103**, 207601 (2009).
[14] M. E. Manley, D. L. Abernathy, R. Sahul, D. E. Parshall, J. W. Lynn, A. D. Christianson, P. J. Stonaha, E. D. Specht, and J. D. Budai, Sci. Adv. **2**, e1501814 (2016).
[15] F. Li, S. Zhang, T. Yang, Z. Xu, N. Zhang, G. Liu, J. Wang, J. Wang, Z. Cheng, Z.-G. Ye, J. Luo, T. R. Shrout, and L.-Q. Chen, Nat. Commun. **7**, 13807 (2016).
[16] F. Li, S. Zhang, Z. Xu, and L.-Q. Chen, Adv. Funct. Mater. **27**, 1700310 (2017).
[17] H. Fu and R. E. Cohen, Nature (London, UK) **403**, 281 (2000).
[18] B. Noheda, D. E. Cox, G. Shirane, S.-E. Park, L. E. Cross, and Z. Zhong, Phys. Rev. Lett. **86**, 3891 (2001).
[19] R. R. Chien, V. H. Schmidt, C.-S. Tu, L.-W. Hung, and H. Luo, Phys. Rev. B **69**, 172101 (2004).
[20] Z. Kutnjak, J. Petzelt, and R. Blinc, Nature (London, UK) **441**, 956 (2006).
[21] Z. Kutnjak, R. Blinc, and Y. Ishibashi, Phys. Rev. B **76**, 104102 (2007).
[22] F. Li, S. Zhang, Z. Xu, X. Wei, J. Luo, and T. R. Shrout, Appl. Phys. Lett. **96**, 192903 (2010).
[23] D. Hou, T.-M. Usher, L. Fulanovic, M. Vrabelj, M. Otonicar, H. Ursic, B. Malic, I. Levin, and J. L. Jones, Phys. Rev. B **97**, 214102 (2018).
[24] S. Aoyagi, H. Osawa, K. Sugimoto, A. Fujiwara, S. Takeda, C. Moriyoshi, and Y. Kuroiwa, Appl. Phys. Lett. **107**, 201905 (2015).
[25] S. Aoyagi, H. Osawa, K. Sugimoto, S. Takeda, C. Moriyoshi, and Y. Kuroiwa, Jpn. J. Appl. Phys. **55**, 10TC05 (2016).
[26] S. Aoyagi, H. Osawa, K. Sugimoto, Y. Nakahira, C. Moriyoshi, Y. Kuroiwa, H. Takeda, and T. Tsurumi, Jpn. J. Appl. Phys. **57**, 11UB06 (2018).
[27] S. Aoyagi, H. Osawa, K. Sugimoto, M. Iwata, S. Takeda, C. Moriyoshi, and Y. Kuroiwa, Jpn. J. Appl. Phys. **54**, 10NB03 (2015).
[28] K. Sugimoto, H. Ohsumi, S. Aoyagi, E. Nishibori, C. Moriyoshi, Y. Kuroiwa, H. Sawa, and M. Takata, in *SRI 2009, 10th International Conference on Radiation Instrumentation—2009, Melbourne*, AIP Conf. Proc. No. 1234, edited by R. Garrett, I. Gentle, K. Nugent, and S. Wilkins (AIP, New York, 2010), p. 887.
[29] H. Osawa, T. Kudo, and S. Kimura, Jpn. J. Appl. Phys. **56**, 048001 (2017).
[30] M. Ozgul, K. Takemura, S. Trolier-McKinstry, and C. A. Randall, J. Appl. Phys. **89**, 5100 (2001).
[31] B. Noheda, Z. Zhong, D. E. Cox, G. Shirane, S.-E. Park, and P. Rehrig, Phys. Rev. B **65**, 224101 (2002).
[32] M. Davis, D. Damjanovic, and N. Setter, Phys. Rev. B **73**, 014115 (2006).
[33] J. Yin, B. Jiang, and W. Cao, IEEE Trans. Ultrason., Ferroelectr., Freq. Control **47**, 285 (2000).
[34] C. Kwamen, M. Rössle, M. Reinhardt, W. Leitenberger, F. Zamponi, M. Alexe, and M. Bargheer, Phys. Rev. B **96**, 134105 (2017).
[35] S. Gorfman, H. Choe, V. V. Shvartsman, M. Ziolkowski, M. Vogt, J. Strempfer, T. Łukasiewicz, U. Pietsch, and J. Dec, Phys. Rev. Lett. **114**, 097601 (2015).
[36] G. M. Sheldrick, Acta Crystallogr., Sect. C: Struct. Chem. **71**, 3 (2015).
[37] M. E. Marssi and H. Dammak, Solid State Commun. **142**, 487 (2007).